

# Consecutive Ruptures on a Complex Conjugate Fault System During the 2018 Gulf of Alaska Earthquake

Shinji Yamashita<sup>1,\*</sup>, Yuji Yagi<sup>2,\*\*</sup>, Ryo Okuwaki<sup>2,3,4</sup>, Kousuke Shimizu<sup>1</sup>, Ryoichiro Agata<sup>5</sup>, and Yukitoshi Fukahata<sup>6</sup>

<sup>1</sup>Graduate School of Life and Environmental Sciences, University of Tsukuba, Tsukuba, Ibaraki 305-8572, Japan

<sup>2</sup>Faculty of Life and Environmental Sciences, University of Tsukuba, Tsukuba, Ibaraki 305-8572, Japan

<sup>3</sup>Mountain Science Center, University of Tsukuba, Ibaraki 305-8572, Japan

<sup>4</sup>COMET, School of Earth and Environment, University of Leeds, Leeds LS2 9JT, UK

<sup>5</sup>Japan Agency for Marine-Earth Science and Technology, 3173-25 Showa-machi, Kanazawa-ku, Yokohama 236-0001, Japan

<sup>6</sup>Disaster Prevention Research Institute, Kyoto University, Uji, Kyoto 611-0011, Japan

\*Corresponding author: Shinji Yamashita ([syamashita@geol.tsukuba.ac.jp](mailto:syamashita@geol.tsukuba.ac.jp))

\*\*Second corresponding author: Yuji Yagi ([yagi-y@geol.tsukuba.ac.jp](mailto:yagi-y@geol.tsukuba.ac.jp))

## ABSTRACT

We developed a flexible finite-fault inversion method for teleseismic  $P$  waveforms to obtain a detailed rupture process of a complex multiple-fault earthquake. We estimate the distribution of potency-rate density tensors on an assumed model fault plane to clarify rupture evolution processes, including variations of fault geometry. We applied our method to the 23 January 2018 Gulf of Alaska earthquake, setting the model fault area to fit the distribution of aftershocks occurring within one week of the mainshock. The obtained source model, which successfully explained the complex teleseismic  $P$  waveforms, shows that the 2018 earthquake ruptured a conjugate system of N-S and E-W faults. The spatiotemporal rupture evolution indicates irregular rupture behavior involving a multiple-shock sequence, which is likely associated with discontinuities in the fault geometry that originated from E-W sea-floor fracture zones and N-S plate-bending faults.

## Introduction

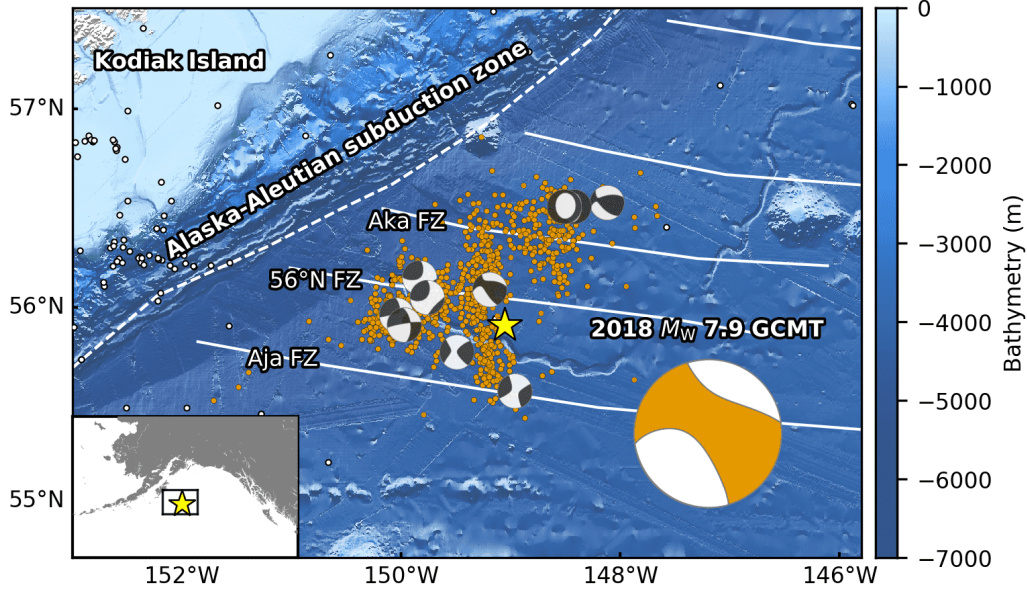
The 23 January 2018 Gulf of Alaska earthquake (moment-magnitude  $M_w$  7.9<sup>1</sup>) struck offshore Kodiak Island (55.9097°N, 149.0521°W, 10.4 km depth; Alaska Earthquake Information Center, AEIC<sup>1</sup>), in the seaward-region of the Alaska-Aleutian subduction zone. The Global Centroid Moment Tensor (GCMT) project<sup>2,3</sup> reported that the 2018 Alaska earthquake had strike-slip faulting with a large non-double-couple component (47%). Aftershock seismicity determined by the AEIC<sup>1</sup> shows a lineation extending about 120 km N-S near the epicenter and two aftershock clusters centered about 60 km northeast and about 50 km west from the epicenter (Fig. 1). The GCMT solutions of aftershocks are dominated by strike-slip faulting, but include normal and reverse faulting (Fig. 1).

39 Several pioneering studies that built finite-fault models based on the aftershock distribution  
40 demonstrated that the 2018 Alaska earthquake ruptured a quasi-orthogonal multiple-fault system  
41 oriented approximately N-S and E-W<sup>4-8</sup>. However, it is difficult to adopt a reasonable fault model  
42 because the fault model parametrization, number of fault segments, and fault geometries differ by  
43 study, partly due to the spatial spread of the aftershock distribution (Fig. 1). Based on the static  
44 slip distribution estimated from Global Navigation Satellite System and tsunami data, major slips  
45 occurred on E-W-striking segments<sup>5,7,8</sup>. Finite-fault inversions estimated that the maximum slip  
46 occurred around the boundary between the crust and uppermost mantle in the N-S-oriented  
47 segment<sup>4,6</sup>, which would have played a significant role in tsunami generation. However, it remains  
48 challenging to adequately explain the complex characteristics of the observed teleseismic body  
49 waveforms by conventional finite-fault inversion methods due to the uncertainty on the fault  
50 geometry, which lead to significant model errors.

51 In the framework of finite-fault waveform inversion, uncertainties on the Green's function  
52 and fault geometry have been the major sources of model errors<sup>9-13</sup>. Those due to uncertainty on  
53 the Green's function arose from a discrepancy between the true and calculated Green's functions.  
54 To mitigate the effect of this uncertainty, Yagi and Fukahata<sup>13</sup> explicitly introduced the error term  
55 of the Green's function into the data covariance matrix. As a result, their inversion framework  
56 allowed the stable estimation of the spatiotemporal distribution of slip-rate, usually without the  
57 non-negative slip-rate constraint, which had been commonly applied in conventional waveform  
58 inversion methods to obtain a plausible solution<sup>14,15</sup>.

59 Model errors due to uncertainty on the fault geometry arose from inappropriate  
60 assumptions about the fault geometry<sup>11,12</sup>. For strike-slip earthquakes, many seismic stations are  
61 distributed in the vicinity of nodal planes where the radiation pattern is sensitive to the assumed  
62 fault geometry. An obtained solution can easily be distorted by inappropriate assumptions of strike  
63 and dip<sup>12</sup>. These effects can be mitigated by increasing the degrees of freedom in the assumed  
64 seismic source model. Shimizu et al.<sup>12</sup> proposed an inversion method to express slip vectors on  
65 the assumed model plane as the seismic potency tensor. Because their method adopts a linear  
66 combination of five basis double-couple components<sup>16</sup>, the slip direction is not restricted to the  
67 two slip components compatible with the fault direction. Of course, the true fault geometry should  
68 be compatible with the actual slip direction. Nonetheless, because the teleseismic *P*-wave Green's  
69 function is insensitive to slight changes in the absolute source location, their inversion method  
70 enabled the spatiotemporal resolution of not only the detailed rupture evolution, but also variation  
71 of the focal mechanism, including information on the fault geometry, which may differ from the  
72 assumed model plane.

73 In this study, we developed a flexible finite-fault inversion framework that can estimate  
74 both the rupture evolution and focal mechanism of earthquakes that ruptured along multiple  
75 complex fault segments. This method incorporates appropriate smoothness constraints and a high-  
76 degree-of-freedom planar model into the inversion framework of Shimizu et al.<sup>12</sup>. Application of  
77 our framework to the 2018 Alaska earthquake shows that our source model sufficiently reproduced  
78 the observed complex waveforms without assumptions on fault geometry. The model also clarified  
79 multiple, distinct rupture events in the conjugate fault system that have not been revealed by  
80 conventional finite-fault inversion methods.



81

82 **Figure 1.** Overview of the source region of the 2018 Gulf of Alaska earthquake. The star is the  
 83 mainshock epicenter, orange dots are aftershocks ( $M \geq 3$ ) that occurred within one week of the  
 84 mainshock, and white dots show background seismicity before the mainshock ( $M \geq 3.5$ , 1 January  
 85 2008 to 22 January 2018); all epicentral locations are from AEIC<sup>1</sup>. The ‘beachball’ diagrams show  
 86 the GCMT solutions for the mainshock (large, bottom right) and aftershocks with  $M \geq 3.5$ . White  
 87 dashed lines represent plate boundaries<sup>44</sup>, and white solid lines represent fracture zones<sup>45,46</sup>. The  
 88 background bathymetry is derived from the GEBCO 2020 Grid<sup>47</sup>. The inset map shows the  
 89 regional setting.

## 90 Method

91 In the inversion framework of Shimizu et al.<sup>12</sup>, the seismic waveform  $u_j$  observed at a station  $j$  is  
 92 given by

$$93 \quad u_j(t) = \sum_{q=1}^5 \int_S (G_{qj}(t, \xi) + \delta G_{qj}(t, \xi)) * \dot{D}_q(t, \xi) d\xi + e_{bj}(t), \quad (1)$$

94 where  $G_{qj}$  is the calculated Green’s function of the  $q$ th basis double-couple component,  $\delta G_{qj}$  is  
 95 the model error on  $G_{qj}$ <sup>13</sup>,  $\dot{D}_q$  is the  $q$ th potency-rate density function on the assumed fault model  
 96 plane  $S$ ,  $e_{bj}$  is background and instrumental noise,  $\xi$  represents a position on  $S$ , and  $*$  denotes the  
 97 convolution operator in the time domain.

98 Shimizu et al.<sup>12</sup> represented the assumed fault model plane  $S$  as a rectangle horizontally  
 99 covering the seismic source region. However, for earthquakes with complex fault geometries, such  
 100 as the 2018 Alaska earthquake, such a horizontal rectangular model plane includes areas beyond  
 101 the seismic source region. Therefore, we further extended their inversion framework such that a  
 102 horizontal non-rectangular model plane can be set according to the shape of the ruptured region as  
 103 estimated from other information (e.g., aftershock seismicity). In other words, we introduced *a*  
 104 *priori* information about the possible ruptured area into the inversion framework. In numerical

105 tests, the use of a non-rectangular model plane improved spatial resolution and computation costs  
 106 compared to a rectangular one (see Supplementary Material S1 and Figs. S1–S4).

107 In general, inversions are stabilized by adding smoothness constraints either implicitly or  
 108 explicitly<sup>17,18</sup>. In the formulation of Shimizu et al.<sup>12</sup>, the smoothness constraints on each potency-  
 109 rate density function  $\dot{D}_q$  in space and time are represented as

$$110 \quad \nabla^2 \dot{D}_q(t, \xi) + \alpha_q = 0, \quad (2)$$

$$111 \quad \frac{\partial^2}{\partial t^2} \dot{D}_q(t, \xi) + \beta_q = 0, \quad (3)$$

112 where  $\alpha_q$  and  $\beta_q$  are assumed to be Gaussian noise with zero mean and covariances of  $\sigma^2 \mathbf{I}$  and  
 113  $\tau^2 \mathbf{I}$ , respectively, where  $\mathbf{I}$  is an  $M \times M$  ( $M$  is the number of model parameters) unit matrix.  
 114 Because they introduced identical Gaussian distributions for all basis components and determined  
 115 the optimal values of the hyperparameters  $\sigma^2$  and  $\tau^2$  by Akaike's Bayesian information criterion  
 116<sup>18,19</sup>, the potency-rate density functions of basis components with relatively high amplitudes  
 117 become smoother than those of basis components with relatively low amplitudes, which may bias  
 118 the solution. Thus, when the amplitudes of the potency-rate density functions differ for each basis  
 119 component, the standard deviations of the smoothness constraints should depend on the amplitude  
 120 of each basis component.

121 In this study, we set the standard deviation of the smoothness constraints for each basis  
 122 double-couple component to be proportional to its amplitude. That is, instead of  $\alpha_q$  and  $\beta_q$ , we  
 123 directly introduced Gaussian noise with zero mean and covariances  $\sigma_q^2 \mathbf{I}$  and  $\tau_q^2 \mathbf{I}$ , respectively, as

$$124 \quad \sigma_q^2 \mathbf{I} = k^2 m_q^2 \sigma^2 \mathbf{I}, \quad (4)$$

$$125 \quad \tau_q^2 \mathbf{I} = k^2 m_q^2 \tau^2 \mathbf{I}, \quad (5)$$

126 where  $k$  is a scaling factor and  $m_q$  is the total potency of the  $q$ th basis double-couple component,  
 127 which is independently derived from the moment tensor solution. To avoid extremely small  
 128 standard deviations destabilizing the solution, we adjusted  $k|m_q|$  so that it does not fall below  
 129 10% of its maximum absolute value. Following Yagi and Fukahata<sup>13</sup>, we determined the  
 130 hyperparameters  $\sigma^2$  and  $\tau^2$  by Akaike's Bayesian information criterion<sup>18,19</sup>. In numerical tests,  
 131 these improved smoothness constraints mitigated the excessive smoothing of the dominant basis  
 132 component imposed by conventional smoothness constraints and, when combined with a non-  
 133 rectangular model plane, outperformed the conventional framework (see Supplementary Material  
 134 S1, Figs. S1–S4 and Table S1).

### 135 Data and Fault Parameterization

136 We used teleseismic  $P$  waveforms (vertical components) recorded at stations with epicentral  
 137 distances of 30–90° (downloaded from the Incorporated Research Institutions for Seismology Data  
 138 Management Center). Of these, we selected 78 stations with good data quality and azimuthal  
 139 coverage (Fig. 2c) and converted the  $P$  waveforms to velocity waveforms at a sampling rate of 0.8  
 140 s. The theoretical Green's functions for teleseismic body waves were calculated by the method of  
 141 Kikuchi and Kanamori<sup>16</sup> at a sampling rate of 0.1 s, and the attenuation time constraint  $t^*$  for the  
 142  $P$  wave was taken to be 1.0 s. We adopted a 1-D velocity structure derived from the CRUST1.0  
 143 model<sup>20</sup> (see Supplementary Table S2) to calculate the theoretical Green's functions. Following

144 Shimizu et al. <sup>12</sup>, we did not low-pass filter the observed waveforms or calculated Green's  
145 functions. For the smoothness constraints, we calculated  $m_q$  based on the GCMT solution of the  
146 2018 Alaska earthquake. The GCMT solution shows that the M1 (strike-slip) component <sup>16</sup> is more  
147 prominent than the others (see Supplementary Table S3), including the M4 (dip-slip) component  
148 <sup>16</sup> (see Supplementary Fig. S4). The scaling factor  $k$  in eqs. (4) and (5) was set such that  
149  $\min(k|m_q|) = 1$  (Table S3).

150 Based on the aftershock distribution, the 2018 Alaska earthquake is considered to have  
151 occurred on a quasi-orthogonal multiple-fault system <sup>4-8</sup>. To cover the high point density area of  
152 aftershocks within one week of the event <sup>1</sup> (Fig. 2a), we set up a non-rectangular horizontal model  
153 fault plane with a maximum width and length of 130 km, which was expanded using a bilinear B-  
154 spline with a knot spacing of 10 km. We adopted the epicenter as that determined by the AEIC <sup>1</sup>:  
155 55.9097°N, 149.0521°W. The depth of the model fault plane was set at 33.6 km according to the  
156 GCMT centroid depth. For the inversion analysis, we adopted a potency-rate density function on  
157 each knot, each representing a linear combination of B-splines at an interval of 0.8 s. The  
158 maximum rupture-front velocity, which defines the rupture starting time at each knot, was set to  
159 7.0 km/s to account for the possibility of supershear rupture propagation. The rupture ending time  
160 at each knot was set to 65 s from the origin time based on previous inversion results <sup>4,6</sup>. We  
161 evaluated the sensitivity of our model by perturbing the model parameters, and the robustness of  
162 the new method (see Supplementary Material S2, and Figs. S5, S6 and S9).

## 163 Results

164 We estimated the spatiotemporal distribution of the potency density tensor for the 2018 Alaska  
165 earthquake by applying our flexible finite-fault inversion method to teleseismic  $P$  waveforms. The  
166 estimated total moment tensor, calculated by taking the spatial and temporal integrals of the  
167 potency-rate density functions, expresses strike-slip faulting, including 36% non-double-couple  
168 components (Fig. 2a). The spatial distribution of the potency density tensor, obtained by  
169 temporally integrating the potency-rate density functions at each knot, is also dominated by strike-  
170 slip focal mechanisms, with a maximum slip of 6 m about 50 km north of the epicenter (Fig. 2a).  
171 The moment rate function is elevated over two time periods, separated at 27 s from the origin time:  
172 the first period is characterized by three large spikes and the second by numerous smaller spikes  
173 (Fig. 2b). The total seismic moment is  $14.9 \times 10^{20}$  N m ( $M_w$  8.05). The synthetic waveforms from  
174 the obtained source model well reproduce the observed waveforms (see Supplementary Fig. S11),  
175 including those at stations near the nodal planes (Fig. 2d).

176 Based on the moment rate function and snapshots of the potency-rate density tensors (Figs.  
177 2b and S12, respectively), we report the detailed rupture history by dividing it into main (A, 0–27  
178 s) and secondary rupture stages (B, 27–65 s). Based on the location, timing, and continuity of the  
179 rupture, we further identified three phases (A1–A3) during the main stage and five (B1–B5) during  
180 the secondary stage.

### 181 Main Rupture Stage (A)

182 The initial phase, A1 (0–9 s), started at the hypocenter and propagated bilaterally northward and  
183 southward with strike-slip focal mechanisms (snapshot at 2 s in Fig. 3a). Although it is generally  
184 difficult to identify the preferred fault plane from the two possible nodal planes in this earthquake,  
185 the direction of rupture propagation during phase A1 coincided with the N-S directed nodal plane.  
186 The spatial distribution of focal mechanisms shows that the strike of the fault plane gradually

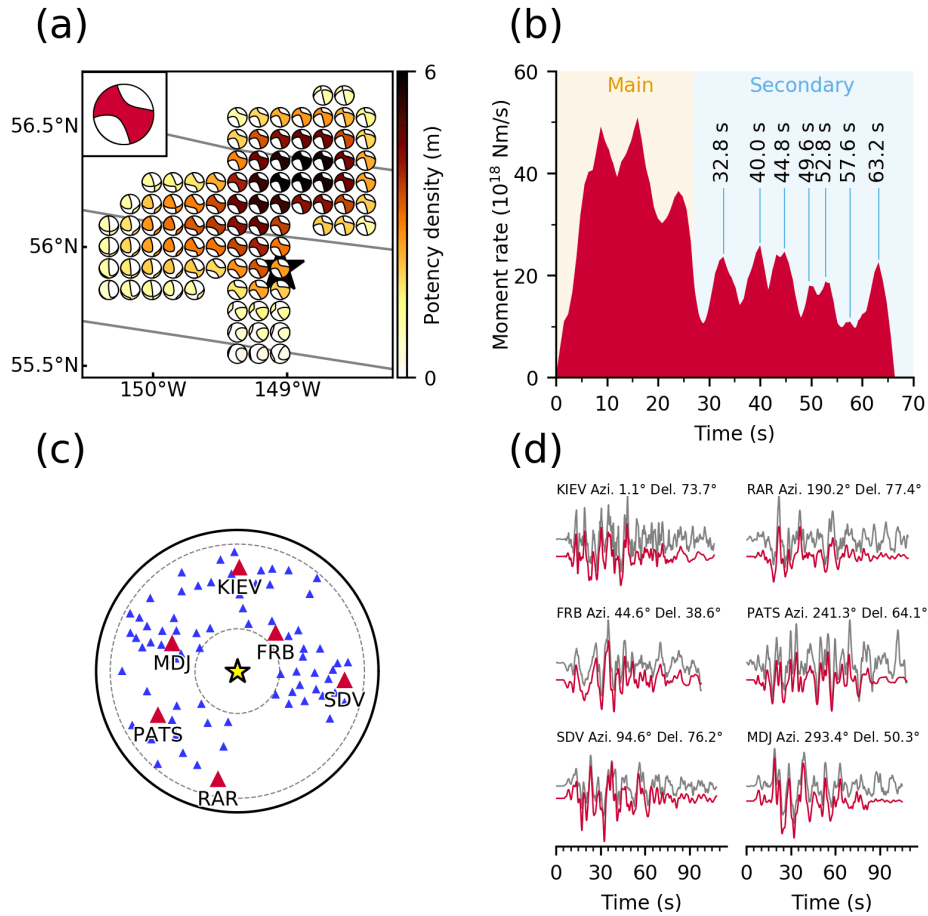
187 rotated counterclockwise from north to south of the epicenter; we obtained a strike/dip of  $174^{\circ}/82^{\circ}$   
188 around 20 km north of the epicenter, but  $163^{\circ}/76^{\circ}$  around 20 km south of the epicenter (6 s in Fig.  
189 3a). The northward rupture seems to have stagnated near the  $56^{\circ}\text{N}$  fracture zone <sup>21</sup> (FZ) after about  
190 9 s .

191 Phase A2 (7–27 s) started about 50 km northeast of the epicenter at around 7 s after the  
192 origin time and propagated west along the Aka FZ <sup>21</sup> (8 s in Fig. 3a). This rupture direction is  
193 consistent with the obtained E-W strike directions (e.g., 10 s in Fig. 3a). The westward rupture  
194 propagated to  $149.2^{\circ}\text{W}$ , where the Aka FZ intersects the N-S aftershock lineation, until 11 s, then  
195 turned southward, indicating that the N-S strike direction is the preferred fault plane (12 s in Fig.  
196 3a). The southward rupture halted at around 12 s at the same location where the northward rupture  
197 of phase A1 had stagnated at about 9 s. After 12 s, a discontinuous rupture occurred along the Aka  
198 FZ: ruptures propagating southward and northward from the Aka FZ near  $148.6^{\circ}\text{W}$  are detected at  
199 around 16 and 20 s, respectively (Fig. 3a). The rupture on the Aka FZ near  $149.2^{\circ}\text{W}$  is again  
200 apparent at around 24 s, and gradually ceased by 27 s.

201 Phase A3 (16–27 s), started about 40 km northwest of the epicenter, near the  $56^{\circ}\text{N}$  FZ,  
202 around 16 s after the origin time (Fig. 3a). This rupture propagated bilaterally to the northeast and  
203 southwest until around 18 s, then gradually abated until around 20 s. At that time, another western  
204 rupture occurred at the northwest end of the model region and propagated to the south (20 s in Fig.  
205 3a), stagnating at the  $56^{\circ}\text{N}$  FZ about 50 km west of the epicenter at around 22 s (24 s in Fig. 3a).

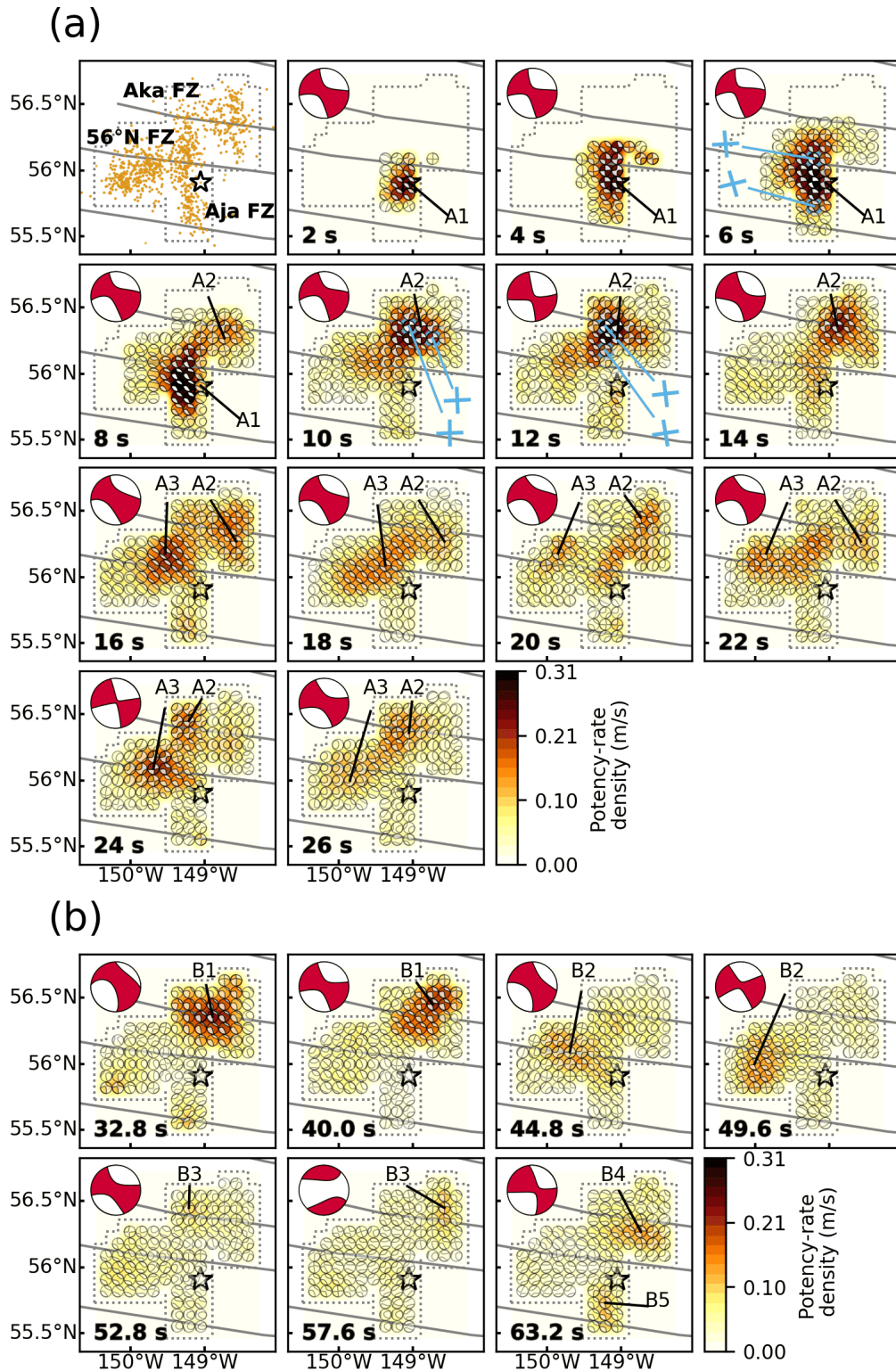
## 206 Secondary Rupture Stage (B)

207 We identified seven peaks in the moment rate function during the secondary rupture stage (Fig.  
208 2b), which we attribute to five phases in the snapshots (Fig. 3b). Phase B1 (28–44 s) occurred  
209 along the Aka FZ. In particular, phase B1 ruptures at around 32.8 and 40.0 s were relatively large,  
210 and appear as individual peaks in the moment rate function (Figs. 2b and 3b). Phase B2 (44–52 s)  
211 mainly ruptured the region west of the epicenter. The rupture at around 44.8 s occurred along the  
212  $56^{\circ}\text{N}$  FZ and that at around 49.6 s struck about 30 km south of the  $56^{\circ}\text{N}$  FZ (Fig. 3b). Phase B3  
213 (53–60 s) occurred mainly northeast of the epicenter, but also struck the intersection of the Aka  
214 FZ and the N-S aftershock lineation at around 52.8 s (Fig. 3b). A northward rupture from the Aka  
215 FZ was also detected at around 57.6 s. The last peak of the moment rate function corresponds to  
216 two independent phases that occurred at around 63.2 s: B4 (62–65 s) ruptured about 20 km south  
217 of the Aka FZ and B5 (62–64 s) ruptured about 30 km south of the epicenter (Fig. 3b).



218

219 **Figure 2.** Model setting and summary of results. (a) Map projection of the potency density tensor  
 220 distribution on the assumed model fault plane. The star and solid lines indicate the epicenter<sup>1</sup> and  
 221 fracture zones<sup>45,46</sup>, respectively. Inset is the total moment tensor. (b) The moment rate function is  
 222 divided into the main and secondary rupture stages at 27 s. The individual peaks during the  
 223 secondary stage correspond to snapshots in Fig. 3b. (c) Azimuthal equidistant projection of the  
 224 station distribution used in the inversion. The star denotes the epicenter, and triangles denote  
 225 station locations (waveforms for red stations are shown in (d)). The inner and outer dotted lines  
 226 show epicentral distances of 30° and 90°, respectively. (d) Comparison of observed waveforms  
 227 (gray) with synthetic waveforms (red) at the selected stations in (c). Each panel is labeled with the  
 228 station name, azimuth (Azi.), and epicentral distance (Del.) from the mainshock. Waveform  
 229 comparisons for all stations are shown in Supplementary Fig. S11.



230

231 **Figure 3.** Snapshots of the potency-rate density tensors for (a) the main rupture stage A and (b)  
 232 the secondary rupture stage B. The corresponding time after onset for each snapshot is noted at the  
 233 bottom-left of each panel. The dotted line shows the border of the assumed model fault plane. The

234 star and solid lines indicate the epicenter <sup>1</sup> and fracture zones <sup>45,46</sup>, respectively. Blue crosses show  
235 the strike directions of small beachball diagrams derived from the potency-rate density tensor. The  
236 top-left panel in (a) is the epicentral distribution of aftershocks ( $M \geq 3$ ) that occurred within one  
237 week of the mainshock <sup>1</sup>. The large beachball in each panel indicates the corresponding total  
238 moment tensor at each time.

## 239 Discussion

240 Our inversion results indicate that the main rupture stage (0–27 s after origin) affected segments  
241 oriented both N-S and E-W, suggesting that the 2018 Alaska earthquake ruptured a conjugate fault  
242 system, as proposed in previous studies <sup>4–8</sup>. Our source model suggests that the rupture occurred  
243 along weak zones in the sea floor: fracture zones extending E-W and plate-bending faults parallel  
244 to N-S magnetic lineaments <sup>22,23</sup>. The N-S plate bending faults have been interpreted as pre-  
245 existing oceanic spreading features that were reactivated by subduction of the Pacific Plate <sup>23</sup>.  
246 Krabbenhoef et al. <sup>21</sup> associated these pre-existing features with the radiation of high-frequency  
247 waves based on back-projection and the aftershock distribution.

248 A notable irregular rupture propagation highlighted by our inversion results is the  
249 northward rupture at around 9 s in phase A1 and the southward rupture at around 12 s in phase A2,  
250 both of which stopped near the 56°N FZ (8 and 12 s, respectively, in Fig. 3a). The N-S aftershock  
251 lineation is divided into northern and southern clusters across the 56°N FZ (Fig. 3a). Given the  
252 phase A1 and A2 ruptures and the geometrical offset of the N-S aftershock lineation, the northern  
253 and southern fault system crossing the 56°N FZ can be regarded as a strike-slip step over. Based  
254 on our obtained focal mechanisms, these two N-S faults are both right-lateral strike-slip faults that  
255 dip steeply to the west (8 and 12 s in Fig. 3a), and the counterclockwise rotation of the strike angle  
256 during phase A1 is consistent with the southern N-S aftershock lineation (6 s in Fig. 3a). Because  
257 irregular rupture behaviors are generally a result of geometric complexities, including barriers  
258 caused by discontinuous fault steps <sup>24–26</sup>, we interpret that this fault step over caused the rupture to  
259 stagnate at around 9 and 12 s.

260 Multiple sub-events occurring in a conjugate strike-slip fault system have been reported in  
261 previous studies <sup>27–31</sup>. In this study, we have shown a causal link between the multiple rupture  
262 episodes during the 2018 Alaska earthquake (stages A and B) and pre-existing bathymetric features  
263 by resolving both the rupture evolution and variation of fault geometry using only teleseismic body  
264 waves. Similar observations were made during the  $M_w$  8.6 2012 Sumatra earthquake in the  
265 Wharton basin. That earthquake involved multiple  $M_w > 8$  sub-events along a conjugate fault  
266 system <sup>30,32</sup>, which developed by deep ductile shear localization beneath the brittle upper  
267 lithosphere of the oceanic plate <sup>33</sup>.

268 We evaluated how the newly developed method improved the source model of the 2018  
269 Gulf of Alaska earthquake by performing the inversion analysis with the conventional smoothness  
270 constraints <sup>12</sup> (Fig. S7). The inversion result with the conventional smoothness constraints show  
271 general agreement with that obtained by the improved smoothness constraints (Fig. S7). However,  
272 the spatiotemporal rupture propagation of the conventional smoothness constraints is smoother  
273 than that of the improved ones by the excessive smoothing for the most dominant  $M1$  component  
274 for the earthquake (Fig. S8), which provides the blurrier image, making it difficult to clearly  
275 resolve the multiple sub-events (Figs. 3 and S7).

276 It is possible that the complex waveforms observed during the 2018 Alaska earthquake  
277 were contaminated by reverberations due to the bathymetric setting that cannot be reproduced by  
278 the theoretical Green's function, resulting in dummy multiple events<sup>34–37</sup>. We evaluated this  
279 possibility by using empirical Green's functions<sup>38,39</sup> and confirm that it is unlikely that the multiple  
280 rupture stages originated from such reverberations (see Supplementary Material S3 and Fig. S10).

281 The sub-events that occurred after the main A1 phase can be regarded as early aftershocks  
282 missing from global catalogs<sup>40</sup>. Although it is difficult to distinguish whether such early near- to  
283 intermediate-field aftershocks were dynamically or statically triggered<sup>40</sup>, it is noteworthy that the  
284 rupture propagated from A1 to A2 at more than 5 km/s (see Supplementary Material S2 and Fig.  
285 S6); this is faster than the surface wave velocity (3–4 km/s), suggesting that the A2 rupture was  
286 triggered by the A1 rupture.

## 287 Conclusions

288 We developed a finite-fault inversion method for teleseismic *P* waveforms with improved  
289 smoothness constraints to obtain source processes for earthquakes with complex multiple-fault  
290 ruptures. We applied our inversion method to the 2018 Alaska earthquake and estimated its  
291 spatiotemporal rupture process. Although the observed waveforms are very complicated, reflecting  
292 the complex rupture process and fault geometry, the waveforms calculated from our source model  
293 fit well. The obtained source model suggests a complex multiple-shock sequence on a conjugate  
294 fault system, consistent with pre-existing bathymetric features. Irregular rupture stagnation about  
295 20 km north of the epicenter may have been promoted by a fault step across a sea-floor fracture  
296 zone.

## 297 References

- 298 1. U.S. Geological Survey Earthquake Hazards Program. Advanced National Seismic  
299 System (ANSS) Comprehensive Catalog of Earthquake Events and Products. (2017)  
300 doi:10.5066/F7MS3QZH.
- 301 2. Dziewonski, A. M., Chou, T.-A. & Woodhouse, J. H. Determination of earthquake source  
302 parameters from waveform data for studies of global and regional seismicity. *J. Geophys.*  
303 *Res. Solid Earth* **86**, 2825–2852 (1981).
- 304 3. Ekström, G., Nettles, M. & Dziewoński, A. M. The global CMT project 2004-2010:  
305 Centroid-moment tensors for 13,017 earthquakes. *Phys. Earth Planet. Inter.* **200–201**, 1–9  
306 (2012).
- 307 4. Guo, R. *et al.* The 2018  $M_w$  7.9 Offshore Kodiak, Alaska, Earthquake: An Unusual Outer  
308 Rise Strike-Slip Earthquake. *J. Geophys. Res. Solid Earth* **125**, (2020).
- 309 5. Hossen, M. J., Sheehan, A. F. & Satake, K. A Multi-fault Model Estimation from Tsunami  
310 Data: An Application to the 2018  $M7.9$  Kodiak Earthquake. *Pure Appl. Geophys.* **177**,  
311 1335–1346 (2020).
- 312 6. Lay, T., Ye, L., Bai, Y., Cheung, K. F. & Kanamori, H. The 2018  $M_w$  7.9 Gulf of Alaska  
313 Earthquake: Multiple Fault Rupture in the Pacific Plate. *Geophys. Res. Lett.* **45**, 9542–  
314 9551 (2018).
- 315 7. Ruppert, N. A. *et al.* Complex Faulting and Triggered Rupture During the 2018  $M_w$  7.9  
316 Offshore Kodiak, Alaska, Earthquake. *Geophys. Res. Lett.* **45**, 7533–7541 (2018).
- 317 8. Zhao, B. *et al.* Coseismic slip model of the 2018  $M_w$  7.9 gulf of Alaska earthquake and  
318 its seismic hazard implications. *Seismol. Res. Lett.* **90**, 642–648 (2019).

- 319 9. Duputel, Z., Agram, P. S., Simons, M., Minson, S. E. & Beck, J. L. Accounting for  
320 prediction uncertainty when inferring subsurface fault slip. *Geophys. J. Int.* **197**, 464–482  
321 (2014).
- 322 10. Minson, S. E., Simons, M. & Beck, J. L. Bayesian inversion for finite fault earthquake  
323 source models I—theory and algorithm. *Geophys. J. Int.* **194**, 1701–1726 (2013).
- 324 11. Ragon, T., Sladen, A. & Simons, M. Accounting for uncertain fault geometry in  
325 earthquake source inversions – I: theory and simplified application. *Geophys. J. Int.* **214**,  
326 1174–1190 (2018).
- 327 12. Shimizu, K., Yagi, Y., Okuwaki, R. & Fukahata, Y. Development of an inversion method  
328 to extract information on fault geometry from teleseismic data. *Geophys. J. Int.* **220**,  
329 1055–1065 (2020).
- 330 13. Yagi, Y. & Fukahata, Y. Introduction of uncertainty of Green’s function into waveform  
331 inversion for seismic source processes. *Geophys. J. Int.* **186**, 711–720 (2011).
- 332 14. Das, S. & Kostrov, B. V. Inversion for seismic slip rate history and distribution with  
333 stabilizing constraints: Application to the 1986 Andreanof Islands Earthquake. *J.*  
334 *Geophys. Res.* **95**, 6899 (1990).
- 335 15. Hartzell, S. H. & Heaton, T. H. Inversion of strong ground motion and teleseismic  
336 waveform data for the fault rupture history of the 1979 Imperial Valley, California,  
337 earthquake. *Bull. Seismol. Soc. Am.* **73**, 1553–1583 (1983).
- 338 16. Kikuchi, M. & Kanamori, H. Inversion of complex body waves - III. *Bull. - Seismol. Soc.*  
339 *Am.* **81**, 2335–2350 (1991).
- 340 17. Nocquet, J.-M. Stochastic static fault slip inversion from geodetic data with non-negativity  
341 and bound constraints. *Geophys. J. Int.* **214**, 366–385 (2018).
- 342 18. Yabuki, T. & Matsu’ura, M. Geodetic data inversion using a Bayesian information  
343 criterion for spatial distribution of fault slip. *Geophys. J. Int.* **109**, 363–375 (1992).
- 344 19. Akaike, H. Likelihood and the Bayes procedure. *Trab. Estad. Y Investig. Oper.* **31**, 143–  
345 166 (1980).
- 346 20. Laske, G., Masters, G., Ma, Z. & Pasyanos, M. Update on CRUST1.0---A 1-degree global  
347 model of Earth’s crust. *EGU Gen. Assem. 2013* **15**, 2658 (2013).
- 348 21. Krabbenhoft, A., von Huene, R., Miller, J. J., Lange, D. & Vera, F. Strike-slip 23 January  
349 2018 MW 7.9 Gulf of Alaska rare intraplate earthquake: Complex rupture of a fracture  
350 zone system. *Sci. Rep.* **8**, 13706 (2018).
- 351 22. Naugler, F. P. & Wageman, J. M. Gulf of Alaska: Magnetic anomalies, fracture zones, and  
352 plate interaction. *Bull. Geol. Soc. Am.* **84**, 1575–1584 (1973).
- 353 23. Reece, R. S. *et al.* The role of farfield tectonic stress in oceanic intraplate deformation,  
354 Gulf of Alaska. *J. Geophys. Res. Solid Earth* **118**, 1862–1872 (2013).
- 355 24. Aki, K. Characterization of barriers on an earthquake fault. *J. Geophys. Res.* **84**, 6140–  
356 6148 (1979).
- 357 25. Das, S. & Aki, K. Fault plane with barriers: A versatile earthquake model. *J. Geophys.*  
358 *Res.* **82**, 5658–5670 (1977).
- 359 26. Harris, R. A. & Day, S. M. Dynamics of fault interaction: parallel strike-slip faults. *J.*  
360 *Geophys. Res.* **98**, 4461–4472 (1993).
- 361 27. Fukuyama, E. Dynamic faulting on a conjugate fault system detected by near-fault tilt  
362 measurements. *Earth, Planets Sp.* **67**, 38 (2015).

- 363 28. Goldberg, D. E. *et al.* Complex Rupture of an Immature Fault Zone: A Simultaneous  
364 Kinematic Model of the 2019 Ridgecrest, CA Earthquakes. *Geophys. Res. Lett.* **47**,  
365 (2020).
- 366 29. Hudnut, K. *et al.* Surface ruptures on cross-faults in the 24 November 1987 Superstition  
367 Hills, California, earthquake sequence. *Bull. Seismol. Soc. Am.* **79**, 282–296 (1989).
- 368 30. Meng, L. *et al.* Earthquake in a maze: Compressional rupture branching during the 2012  
369 Mw 8.6 Sumatra earthquake. *Science (80-. )*. **337**, 724–726 (2012).
- 370 31. Ross, Z. E. *et al.* Hierarchical interlocked orthogonal faulting in the 2019 Ridgecrest  
371 earthquake sequence. *Science (80-. )*. **366**, 346–351 (2019).
- 372 32. Duputel, Z. *et al.* The 2012 Sumatra great earthquake sequence. *Earth Planet. Sci. Lett.*  
373 **351–352**, 247–257 (2012).
- 374 33. Liang, C., Ampuero, J.-P. & Muñoz, D. P. Deep ductile shear zone facilitates near-  
375 orthogonal strike-slip faulting in a thin brittle lithosphere. *Geophys. Res. Lett.* **n/a**,  
376 e2020GL090744 (2020).
- 377 34. Fan, W. & Shearer, P. M. Coherent Seismic Arrivals in the  $P$  Wave Coda of the 2012  $M_w$   
378 7.2 Sumatra Earthquake: Water Reverberations or an Early Aftershock? *J. Geophys. Res.*  
379 *Solid Earth* **123**, 3147–3159 (2018).
- 380 35. Wiens, D. A. Effects of near source bathymetry on teleseismic P waveforms. *Geophys.*  
381 *Res. Lett.* **14**, 761–764 (1987).
- 382 36. Wiens, D. A. Bathymetric effects on body waveforms from shallow subduction zone  
383 earthquakes and application to seismic processes in the Kurile Trench. *J. Geophys. Res.*  
384 *Solid Earth* **94**, 2955–2972 (1989).
- 385 37. Yue, H., Castellanos, J. C., Yu, C., Meng, L. & Zhan, Z. Localized water reverberation  
386 phases and its impact on backprojection images. *Geophys. Res. Lett.* **44**, 9573–9580  
387 (2017).
- 388 38. Dreger, D. S. Empirical Green’s function study of the January 17, 1994 Northridge,  
389 California earthquake. *Geophys. Res. Lett.* **21**, 2633–2636 (1994).
- 390 39. Hartzell, S. H. Earthquake aftershocks as Green’s functions. *Geophys. Res. Lett.* **5**, 1–4  
391 (1978).
- 392 40. Fan, W. & Shearer, P. M. Local near instantaneously dynamically triggered aftershocks of  
393 large earthquakes. *Science (80-. )*. **353**, 1133–1136 (2016).
- 394 41. Hunter, J. D. Matplotlib: A 2D graphics environment. *Comput. Sci. Eng.* **9**, 90–95 (2007).
- 395 42. Beyreuther, M. *et al.* ObsPy: A python toolbox for seismology. *Seismol. Res. Lett.* **81**,  
396 530–533 (2010).
- 397 43. Wessel, P., Smith, W. H. F., Scharroo, R., Luis, J. & Wobbe, F. Generic mapping tools:  
398 Improved version released. *Eos (Washington, DC)*. **94**, 409–410 (2013).
- 399 44. Bird, P. An updated digital model of plate boundaries. *Geochemistry, Geophys.*  
400 *Geosystems* **4**, (2003).
- 401 45. Matthews, K. J., Miller, R. D., Wessel, P. & Whittaker, J. M. The tectonic fabric of the  
402 ocean basins. *J. Geophys. Res. Solid Earth* **116**, (2011).
- 403 46. Wessel, P. *et al.* Semiautomatic fracture zone tracking. *Geochemistry, Geophys.*  
404 *Geosystems* **16**, 2462–2472 (2015).
- 405 47. GEBCO Bathymetric Compilation Group 2020. GEBCO\_2020 Grid. (2020)  
406 doi:10.5285/a29c5465-b138-234d-e053-6c86abc040b9.  
407

## 408 **Acknowledgments**

409 We thank the editor and the reviewers for evaluating the manuscript. This work was supported by  
410 the Grant-in-Aid for Scientific Research (C) 19K04030. The facilities of IRIS Data Services, and  
411 specifically the IRIS Data Management Center, were used for access to waveforms, related  
412 metadata, and/or derived products used in this study. IRIS Data Services are funded through the  
413 Seismological Facilities for the Advancement of Geoscience (SAGE) Award of the National  
414 Science Foundation under Cooperative Support Agreement EAR-1851048. All the figures were  
415 generated with matplotlib <sup>41</sup> (v3.1.1: <https://doi.org/10.5281/zenodo.3264781>) , ObsPy <sup>42</sup> (1.1.0:  
416 <https://doi.org/10.5281/zenodo.165135>) and Generic Mapping Tools <sup>43</sup>.

## 417 **Author contributions**

418 S.Y. and Y.Y. conceptualized this study, compiled the data and conducted the analyses. S.Y., Y.Y.,  
419 R.O., K.S, R.A. and Y.F. contributed to the methodology. S.Y., Y.Y., R.O. and K.S. processed and  
420 interpreted the data. S.Y. and Y.Y. wrote the manuscript which was revised and edited by R.O.,  
421 K.S., R.A. and Y.F. All authors approved the submitted manuscript. All authors agreed both to be  
422 personally accountable for the author's own contributions and to ensure that questions related to  
423 the accuracy or integrity of any part of the work, even ones in which the author was not personally  
424 involved, are appropriately investigated, resolved, and the resolution documented in the literature.

## 425 **Additional information**

426 Correspondence and requests for materials should be addressed to S.Y. or Y.Y.

## 427 **Data Availability**

428 Waveform data was downloaded through the IRIS Wilber 3 system  
429 ([https://ds.iris.edu/wilber3/find\\_stations/10607586](https://ds.iris.edu/wilber3/find_stations/10607586)). Teleseismic waveforms were obtained from  
430 the following networks: the Canadian National Seismograph Network (CN;  
431 <https://doi.org/10.7914/SN/CN>); the Caribbean USGS Network (CU;  
432 <https://doi.org/10.7914/SN/CU>); the GEOSCOPE (G; <https://doi.org/10.18715/GEOSCOPE.G>);  
433 the Hong Kong Seismograph Network (HK; <https://www.fdsn.org/networks/detail/HK/>); the New  
434 China Digital Seismograph Network (IC; <https://doi.org/10.7914/SN/IC>); the IRIS/IDA Seismic  
435 Network (II; <https://doi.org/10.7914/SN/II>); the International Miscellaneous Stations (IM;  
436 <https://www.fdsn.org/networks/detail/IM/>); the Global Seismograph Network (IU;  
437 <https://doi.org/10.7914/SN/IU>), and the Pacific21 (PS; <https://www.fdsn.org/networks/detail/PS/>).  
438 The moment tensor solutions are obtained from the GCMT catalog  
439 (<https://www.globalcmt.org/CMTsearch.html>). The CRUST 1.0 model is available at  
440 <https://igppweb.ucsd.edu/~gabi/crust1.html>. The fracture zone data is obtained from the Global  
441 Seafloor Fabric and Magnetic Lineation Data Base Project website  
442 (<http://www.soest.hawaii.edu/PT/GSFML/>).  
443  
444